On the effect of the approach velocity on the coalescence of fluid particles

Suat Canberk Ozan*, Hugo Atle Jakobsen

Department of Chemical Engineering, Norwegian University of Science and Technology (NTNU), Trondheim N- 7491, Norway

A B S T R A C T

The effect of the constant relative approach velocity of two Newtonian fluid particles on their coalescence is investigated via a film drainage model. The interfaces are deformable and allowed to have any degree of mobility. The thinning equation is derived based on the lubrication theory, and the tangential velocity of the interface is determined via the Boundary Integral Method (BIM). The details for the treatment of the inherent singularity in BIM are provided. As the approach velocity increases, regardless of the strength of the van der Waals forces and the value of the viscosity ratio (or the degree of the interfacial mobility), three types of behavior of the coalescence time are identified: the linear slow, the dimpled and the multiple-rim drainage regimes. In the first two regions the coalescence time decreases with the approach velocity, eventually passes through a minimum and starts to increase in the third region. The slope in the linear region and the critical velocities separating the regimes are used to quantify the behavior, and given as functions of the Hamaker constant and the viscosity ratio. The results are shown to be in good agreement with several recent experimental studies in the literature.

1. Introduction

Coalescence of fluid particles plays an important role in wide variety of phenomena including natural ones such as the formation of the rain droplets, as well as several processes in chemical and biochemical industries such as food and beverage production or petroleum refining, where multiphase flows are frequently encountered. In these industries, chemical and biochemical reactors, fermentation units, boiling and condensation equipment, and separators are widely employed; the performance and the efficiency of which strongly depend on the characteristics of the dispersed flow within them, i.e., the spatial distribution of the fluid particles in the continuous phase and their size. Therefore, it is crucial to understand the nature of fluid particle coalescence (and breakage) on the scale of the equipment of interest, in which a large number of fluid particles interact at the same time enabling coalescence and breakage to occur simultaneously within the unit. That, however, first requires the understanding of the phenomena on a more fundamental level: the single events of coalescence of two fluid particles, and the breakage of a single particle. In this work, we focus only on the coalescence of two fluid particles, particularly on

the effect of the relative approach velocity of the particles on the coalescence time.

There has been huge interest and effort in gaining better comprehension of coalescence and its effects on multiphase engineering units for decades, which seemingly resulted in some conflicting observations and conclusions. One earlier example of these contradictions might be seen as in between Shinnar and Church (1960), Shinnar (1961) and Howarth (1964). The former claims that immediate coalescence of two fluid particles rarely occurs, but instead the particles rather cohere first entrapping a thin film of continuous phase in between. Whereas, the latter supports the idea of a critical approach velocity, after which immediate coalescence prevails and before which the probability of coalescence is very low. As reviewed by Liao and Lucas (2010), these two proposals lay the foundation for two distinct modeling approaches, the film drainage models and the energy models, respectively. On the other hand, another critical approach velocity is observed by Lehr et al. (2002), after which the collision of the fluid particles result in bouncing instead of coalescence and before which coalescence is rapid. Liao and Lucas (2010) adds Lehr et al. (2002)'s model next to the film drainage and energy models as a third branch. Theoretical estimates that are on the same order of magnitude as Lehr et al. (2002)'s measurement for the critical velocity, are given in the theoretical work of Chesters and Hofman (1982) by

* Corresponding author.
  E-mail address: canberk.ozan@ntnu.no (S.C. Ozan).

Nomenclature

V_{app}	Relative approach velocity of the fluid particles
t_c	Coalescence time
λ_c	Coalescence efficiency
$t_{drainage}$	Drainage time
$t_{contact}$	Contact time
λ	Dispersed to continuous phase viscosity ratio
a	Reduced particle radius
a_1, a_2	Fluid particle radii
h_0	Minimum initial film thickness
μ_d	Dispersed phase viscosity
μ_c	Continuous phase viscosity
R_1, R_2	Fluid particle radii
V_1, V_2	Approach velocities of the particles
r	Radial distance in the film
z	Axial distance in the film
t	Time
h	Thickness of the thin film
$\bar{a}$	Width of the thin film
R_p	Equivalent particle radius
$\bar{h}$	Characteristic measure of film thickness
$\bar{r}$	Characteristic measure of film width
$\varepsilon_1, \varepsilon_2, \epsilon$	Length scale ratios
p	Excess pressure in the film
v_r	r-component of the continuous phase velocity
v_z	z-component of the continuous phase velocity
$\mathbf{v_d}$	Dispersed phase velocity field
p_d	Dispersed phase pressure
U	Tangential velocity of the interface
τ_d	Particle side tangential stress evaluated at the interface
A	Hamaker constant
σ	Surface tension
r_∞	A large radial distance
I	Boundary Integral Method integrand
ρ	Integral variable in radial axis
θ	Azimuth angle
λ^*	Dispersed to continuous phase viscosity ratio multiplied by ϵ
A^*	Dimensionless Hamaker constant
Ca	Capillary number
$\hat{U}$	Tangential velocity of the interface multiplied by λ^*
$\bar{t}$	Characteristic time scale
$Y_1 - Y_4$	Transformed variables employed in spectral element based solvers
δ	A small arbitrary number
R	Radial distance in the polar coordinate system used for singularity treatment
φ	Azimuth angle in the polar coordinate system used for singularity treatment
$[A]$	Integration matrix used for the Boundary Integral equation
V_{dimp}	Critical approach velocity separating the linear and the dimpled drainage regimes
V_{mult}	Critical approach velocity separating the dimpled and the multiple-rim drainage regimes
I_{av}	Averaged Boundary Integral Method integrand
E	Trapezoidal area under $Z\tau_d$ between $[r-\delta, r+\delta]$
Z	Integration kernel
v	Arbitrary scalar quantity
$\hat{v}$	v in Chebyshev pseudospectrum
N	Number of collocation points minus one
T	Matrix relating a quantity and its counterpart on the Chebyshev pseudospectrum based on Chebyshev polynomials
b	Numerical integration vector
$[B]$	Numerical integration matrix
$[C_1] - [C_3]$	Integration matrices employed to compute $[A]$

considering the changes in the kinetic and the surface energies of the particles, and by Kirkpatrick and Lockett (1974) via a film drainage model. Although these studies aim to explain the phenomenon based on different arguments, they are not entirely conflicting, but rather might represent different regions of the particle approach velocity spectrum. Yaminsky et al. (2010) identifies three distinct regimes of coalescence in their experiments with air bubbles in water: at very low approach velocities (smaller than 1 μm/s), the thin film in between bubbles appears to be stable in finite time, at intermediate velocities (upto 150 μm/s) coalescence occurs in the range of 10–100 s with visible dimpling of the interface, and finally at large velocities (much larger than 150 μm/s) almost immediate coalescence is observed with very little hydrodynamic resistance from the film and no observable dimpling. They associate these three regions with DLVO stability meaning that the stability stems from the electrical forces acting between charged interfaces, viscous film drainage in which the film flattens and dimples, and inertial film drainage where coalescence occurs before the deformation of the particles, respectively. Horn et al. (2011) discusses several works from the literature (Chesters and Hofman, 1982; Klaseboer et al., 2000; Yaminsky et al., 2010; Del Castillo et al., 2011) to end up with a single chart of different possible regimes of coalescence as a function of the bubble approach speed and the NaCl concentration in their Figs. 2 and 3. From their map, it is evident that in the limit of zero NaCl concentration, as the approach speed (or the kinetic collision energy) increases sequential regimes of

1. DLVO stability for very low velocity collisions, where no coalescence is possible in finite time;
2. Film drainage governed by viscous effects for collisions with higher velocity, where time of coalescence might be as large as 100 s;
3. Inertia governed rapid film drainage for energetic collisions, where coalescence is virtually immediate;
4. Bouncing regime for even more energetic collisions, where coalescence does not occur;

are expected. However, they do not provide information on how the coalescence time changes within these individual regimes. Orvalho et al. (2015) observes a power-law type relation between the coalescence time, t_c, and the relative approach velocity, V_{app}, in their experiments with air bubbles and liquids of different viscosities. They propose that t_c is a linear function of $V_{app}^{-0.85}$. On the other hand, Del Castillo et al. (2011) observes similar trends in their experiments with air bubbles in pure water, with the additional observation of a minimum in V_{app} versus t_c as the approach velocity further increases.

In the film drainage models, once the fluid particles are brought into contact by the external flow, three consecutive steps are proposed (Shinnar and Church, 1960)

- A thin film of the continuous phase is entrapped in between two colliding particles,
- The film drains until its thickness reaches a critical value,
- The film ruptures and coalescence occurs upon reaching the critical thickness.

If the particles are allowed to be in contact by the external flow for sufficiently long time, such that the time required for the film to drain until the critical thickness is reached, is smaller than the duration of the interaction between the particles, coalescence occurs. Based on the film drainage approach, Coulaloglou (1975) gives a statistical formula for the coalescence efficiency, λ_c, using two characteristic time scales, the drainage and the contact times, as

$$\lambda_c = exp\left(-\frac{t_{drainage}}{t_{contact}}\right) \tag{1}$$

which is frequently employed to estimate coalescence behavior in the scale of the multi-phase equipment such as chemical reactors and separators. The model is restricted to 'gentle' collisions, in which the particles are significantly larger than the radius affected by the collision (or in other words, the width of the emerging thin film) (Chesters, 1991). The energy models, on the other hand, consider more 'energetic' collisions and relates λ_c to the kinetic collision energy and the interfacial energy of the fluid particle instead of $t_{drainage}$ and $t_{contact}$.

To determine the drainage time, $t_{drainage}$, in Eq. (1), numerous models with varying degree of complexity have been proposed in the literature. These models are classified based on the deformability and the tangential mobility of the interfaces (Lee and Hodgson, 1968; Chesters, 1991; Liao and Lucas, 2010). The former classification differentiates between the models for the rigid spherical fluid particles and the ones for the particles with deformable interfaces, which are capable of modeling the experimentally observed dimple formation during the film drainage. In addition to the formation of the dimple, the pimpling, wimpling and rippling of the interface are also possible (Chan et al., 2011). The pimple and the wimple refer to the emergence of an additional rim at the interface, and of a local maximum between the rim and the center of the interface, respectively. Whereas, the development of multiple additional maxima and minima at the interface is termed as rippling. Next, by following Chesters (1991) and Liao and Lucas (2010), the deformable class can be further divided into three subgroups based on the interfacial mobility, as immobile, partially mobile and fully mobile models. Immobile models correspond to the interfaces with zero tangential velocity, which might stem from very high dispersed phase viscosity and/or interfacial tension gradients emerging due to presence of impurities and surfactants (Lee and Hodgson, 1968; Chesters, 1991). In that case, the drainage of the film is governed by viscous forces within the film (resulting in a parabolic velocity profile) and not coupled to the velocity field of the dispersed phase (Liao and Lucas, 2010; Chan et al., 2011). Partially mobile and fully mobile names, on the other hand, are used for the cases where the contribution of the tangential velocity of the interfaces on the film drainage are non-negligible. This non-negligible tangential velocity of the mobile interfaces yields a plug flow-like contribution to the velocity of the film. According to Chesters (1991), for the fully mobile interfaces, the tangential stress at the interface is effectively zero and the drainage is governed either by the deformation or acceleration, respectively corresponding to the viscous and the inertial film drainage regimes. Whereas in the partially mobile interface case the tangential stress at the interface is non-zero and the drainage is controlled by the dispersed phase viscosity. Based on scaling arguments on the thin film in between the fluid particles, Davis et al. (1989) argues that if the dispersed to continuous phase viscosity ratio, λ, is much greater than $\sqrt{a/h_0}$, where $a = \frac{a_1 a_2}{a_1 + a_2}$ is the reduced particle radius, a_1 and a_2 are particle radii, and h_0 is the minimum initial thickness of the film, the fluid particles act as rigid particles, if $\lambda << \sqrt{a/h_0}$ the interfaces of the particles are fully mobile, and if λ and $\sqrt{a/h_0}$ are on comparable magnitudes, the interfaces are partially mobile.

Modeling of the interface as a mobile one, regardless of its deformability, requires the coupling of the flow fields inside the fluid particle and within the film. Davis et al. (1989) employs the Boundary Integral theory to determine the tangential velocity of the interface, which, then, enables the coupling of two velocity fields through the no-slip condition at the interface, without requiring the computation of the velocity profile inside the fluid particle. This approximation lowers the computational efforts significantly and later adapted by many others (Yiantsios and Davis, 1990; 1991; Abid and Chesters, 1994; Saboni et al., 1995; Klaseboer et al., 2000; Bazhlekov et al., 2000). Yiantsios and Davis (1990) concludes that a dimple is always formed during bouyancy-driven interactions between a fluid particle and a surface regardless of the viscosity ratio. In their following work (Yiantsios and Davis, 1991), they extend their work to the interactions between two fluid particles, in the limits of very small and very large interfacial mobilities, and reveal that without the attractive van der Waals forces the coalescence is not possible for deformable interfaces in finite time. They also identify two different rupturing types, the nose and the rim ruptures, which are observed at strong and weak van der Waals forces, respectively. In the nose rupture, the van der Waals forces become significant before dimpling occurs resulting in rupture at the center of the interface, whereas the relatively weaker van der Waals forces allow the capillary forces to act first, resulting in formation of a dimple and a rim away from the axis of symmetry. In that case, the rupture starts from the rim earning the name the rim rupture. Abid and Chesters (1994) and Saboni et al. (1995) study centerline collisions of droplets in the presence of van der Waals forces, assuming a constant approach velocity and a constant droplet interaction force, respectively. They determine the critical film rupture thickness as a function of the Hamaker constant. In their models, the drop viscosity determines the rate of drainage, meaning that the velocity profiles are approximated as plug flows, by neglecting the viscous effects within the film. Klaseboer et al. (2000) compare their experimental results obtained for the coalescence of various liquid-liquid couples to outcomes of two theoretical models, in which the interfaces are deformable and the droplets have a constant relative approach velocity. They conclude that the tangentially immobile interface model, where the velocity in the film is parabolic, fits their experimental data more accurately in comparison to the mobile interface model, where they assume a plug-like flow within the film. They suspect that the possibility of very small amount of surfactants being present in the experiments might be responsible for the immobilization of the interface. Bazhlekov et al. (2000) investigate the effect of the viscosity ratio on the film drainage by considering either constant approach velocity or constant interaction force collisions of two fluid particles. Their model takes both the parabolic and plug-like contributions to the film flow into account, thereby closing the gap between preexisting immobile and mobile models in the literature. They present estimations for the minimum film thickness as a function of time and viscosity ratio in a compact form. However, in their expressions the effect of the van der Waals forces is not considered.

Our models follow those of Bazhlekov et al. (2000)'s and Klaseboer et al. (2000)'s, for the mobile and immobile interfaces, respectively, with the addition of van der Waals effects. The addition of the van der Waals forces to the models makes the estimation of the coalescence time possible. Furthermore, we render our equations dimensionless following a different route to set the relative approach velocity of the particles as a model parameter, in order to investigate its effect on the coalescence time explicitly, together with the effects of the disperse to continuous phase viscosity ratio and Hamaker constant. Although our models are similar to the preexisting ones in the literature, the ability to show the individual effect of the approach velocity on the co-
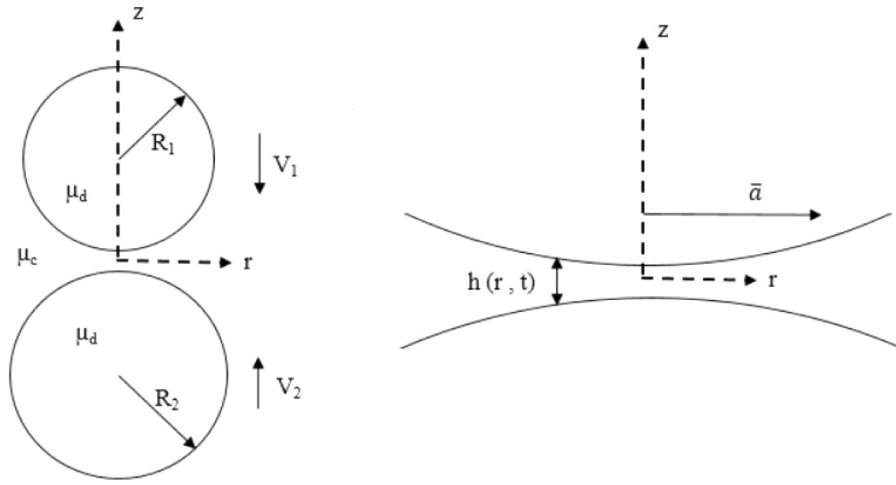
Fig. 1. Physical system.

alescence time directly, enables us to compare our theoretical results to the observations from numerous experimental works such as those of Yaminsky et al. (2010), Del Castillo et al. (2011) and Orvalho et al. (2015), in an efficient and clear manner, thereby allowing us to illuminate some of the missing links between the theoretical and experimental works in the literature.

The article is outlined as follows: The physical configuration of interest and the mathematical model is presented in Section 2. The numerical procedure including the treatment of the singularity inherent to the Boundary Integral Method is given in Section 3. Section 4 presents the coalescence time and the time evolution of the film thickness at different values of the physical parameters of interest, and the comparison of the models' outcome to the experimental observations in the literature. Finally, the conclusions of the work are summarized in Section 5.

2. Physical system and mathematical model

This work considers the axisymmetrical interactions between two Newtonian fluid particles (either droplets or bubbles) of same fluid approaching each other at a constant relative approach velocity, V_{app}, along their centerlines, through a continuous medium of a Newtonian fluid. The depiction of the physical system is presented in Fig. 1. The viscosities of the continuous and the dispersed phases are denoted by μ_c and μ_d, respectively, and the fluid particles are allowed to be of different radii, R_1 and R_2. The interfaces between the dispersed and the continuous phases are immiscible, deformable and characterized by a constant value of surface tension, σ. As the fluid particles approach each other, they entrap a thin film of the continuous phase in between them, which eventually starts to drain. The thickness of this emergent thin film, h, is a function of the radial position r and the time t. It is possible to identify three distinct lengths governing the film drainage phenomenon: the particle radii R_1 and R_2, the thickness of the film $h(r, t)$ and the width of the film $\bar{a}$. Although the characteristic length scales for the first two are straightforward, the width of the film is not easy to measure. Therefore its magnitude will be related to the length scales for the particle size and the film thickness later on during the derivation of the model. Provided that the collision is a gentle one, meaning that both particle radii are much larger than the characteristic film width, the equivalent radius, defined by

$$\frac{1}{R_p} = \frac{1}{2}\left(\frac{1}{R_1} + \frac{1}{R_2}\right) \tag{2}$$

can be used as the length scale for both particles (Chesters, 1991). Due to this approximation, the collision of unequal-sized particles can be modeled as the collision of equal-sized ones, meaning that symmetry around r axis is also introduced to the model in addition to the axisymmetry. This new symmetry creates four equivalent quadrants, enabling us to seek for the solution only in one of them. Here, only the solution in $r \geq 0$, $z \geq 0$ quadrant is sought, where the interface position is given by $z = h(r, t)/2$. The gentle collision resulting in emergence of a thin film suggests a relation between the three length scales:

$$\bar{h} << \bar{a} << R_p \tag{3}$$

where $\bar{h}$ and $\bar{a}$ are measures of the thickness and the width of the film, respectively. In the light of this argument on the length scales, two dimensionless ratios are defined as

$$\frac{\bar{h}}{\bar{a}} = \varepsilon_1 << 1, \qquad \frac{\bar{a}}{R_p} = \varepsilon_2 << 1 \tag{4}$$

which further suggests that a small number ϵ can be defined as

$$\left(\frac{\bar{h}}{R_p}\right)^{1/2} = \sqrt{\varepsilon_1 \varepsilon_2} = \epsilon \tag{5}$$

Then, ϵ can be utilized to relate the three distinct length scales in the model as

$$\bar{h} = \epsilon^2 R_p, \qquad \bar{r} = \sqrt{\frac{\varepsilon_1}{\varepsilon_2}}\bar{a} = \epsilon R_p \tag{6}$$

where, $\bar{r}$ is employed in order to unify the order of magnitude difference between the length scales and hereafter, adopted as the r-direction length scale instead of $\bar{a}$.

2.1. Governing equations and boundary conditions

Based on the arguments in Section 2 ($\bar{h} << \bar{r}$) the lubrication theory is applicable within the film. Following the analysis of Yiantsios and Davis (1990), as $\epsilon = \bar{h}/\bar{r} << 1$, the flow of the film is governed by the simplified versions of the Navier–Stokes and the continuity equations

$$\frac{\partial p}{\partial r} = \mu_c \frac{\partial^2 v_r}{\partial z^2}, \qquad \frac{\partial p}{\partial z} = 0 \tag{7}$$

and

$$\frac{\partial v_z}{\partial z} + \frac{1}{r}\frac{\partial}{\partial r}(r v_r) = 0 \tag{8}$$

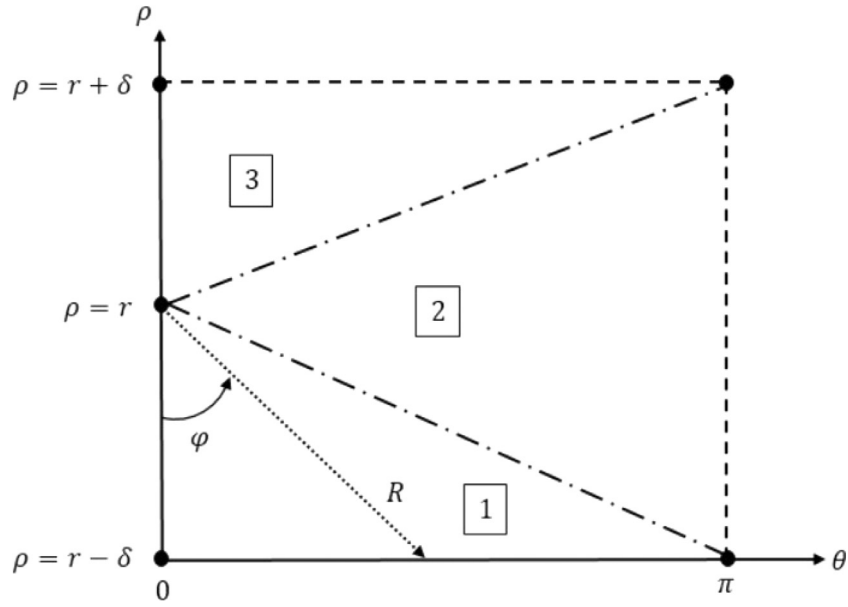**Fig. 2.** Sketch of the coordinate transformation from (ρ, θ) to (R, φ) and the integration domain. Labels 1, 2 and 3 stand for the integration subdomains that have to be handled separately.
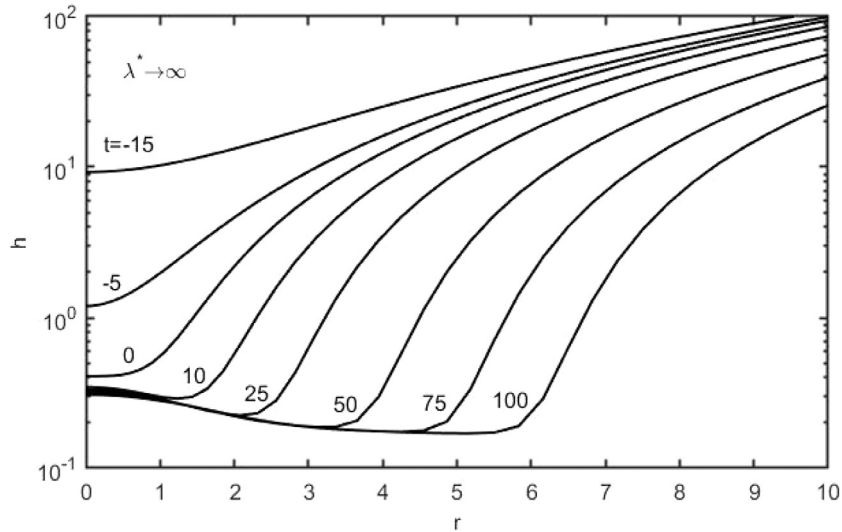

Fig. 3. Fig. 4 of Klaseboer et al. (2000) reproduced for validation of the immobile solver. Thin film thickness as a function of r and t as $\lambda^* \to \infty$. Here, to match Klaseboer et al. (2000), t is shifted by -17 to set the onset of dimpling as $t = 0$. Profiles are obtained with $A^* = 0$, $V_{app} = 1$, $h_{00} = 10$ and $r_\infty = 15$.

where p is the excess pressure in the film, and, v_z and v_r are the z and r components of the continuous phase velocity. The flow within the particles, on the other hand, is approximated by the incompressible Stokes equations

$$\mu_d \nabla^2 \mathbf{v_d} = \nabla p_d \tag{9}$$

and

$$\nabla \cdot \mathbf{v_d} = 0 \tag{10}$$

where p_d and $\mathbf{v_d}$ are the dispersed phase pressure and velocity fields, respectively. The flows in both phases are coupled via a set of boundary conditions valid at the interface, $z = h(r,t)/2$: the no-slip condition, the kinematic condition, and the tangential and the normal components of the stress balance given by

$$v_r|_{z=h/2} = U \tag{11}$$

$$\frac{1}{2}\frac{\partial h}{\partial t} = v_z|_{z=h/2} - \frac{1}{2}\frac{\partial h}{\partial r} v_r|_{z=h/2} \tag{12}$$

$$-\mu_c \left.\frac{\partial v_r}{\partial z}\right|_{z=h/2} = \tau_d \tag{13}$$

$$p = \frac{2\sigma}{R_p} - \sigma\frac{1}{2r}\frac{\partial}{\partial r}\left(r\frac{\partial h}{\partial r}\right) + \frac{A}{6\pi h^3} \tag{14}$$

respectively. The kinematic condition, Eq. (12), appears due to the continuity between the normal component of the velocity of the thin film and the normal speed of the interface (given by $\frac{1}{2}\frac{\partial h}{\partial t}$). Here, U is the tangential velocity of the interface, τ_d is the particle-side tangential stress evaluated at the interface, A is the Hamaker constant, and the deviations in the particle-side pressure are neglected in Eq. (14) due to the gentle collision assumption. Furthermore, it is assumed that at a large enough radial distance, at r_∞, the shape of the interface and the approach velocity are unaffected

by the collision. Then, the conditions,

$$p|_{r=r_\infty} = 0 \qquad \text{and} \qquad \frac{\partial h}{\partial t}\bigg|_{r=r_\infty} = -V_{app} \qquad (15)$$

hold. Eq. (15) form the set of boundary conditions for p and h together with the symmetry conditions at $r = 0$. The initial film thickness is taken as

$$h = h_{00} + \frac{r^2}{R_p} \qquad (16)$$

to resemble the distance between two spherical fluid particles. To determine U, the boundary integral form of the Stokes flow is used (reader may refer to Davis et al. (1989) and Ladyzhenskaya (1969) for further information on the method.)

$$U = \frac{1}{\mu_d} \int_0^{r_\infty} I(\rho, \theta)\, \tau_d\, d\rho \qquad (17)$$

where

$$I(\rho, \theta) = \frac{\rho}{2\pi} \int_0^\pi \frac{cos\theta}{\sqrt{r^2 + \rho^2 - 2r\rho \cos\theta}}\, d\theta \qquad (18)$$

2.2. Dimensionless equations

By applying the transformations

$$\tilde{h} = \frac{h}{\epsilon^2 R_p}, \quad \tilde{r} = \frac{r}{\epsilon R_p}, \quad \tilde{v}_r = \frac{v_r \mu_c}{\epsilon^3 \sigma}, \quad \tilde{v}_z = \frac{v_z \mu_c}{\epsilon^4 \sigma},$$

$$\tilde{V}_{app} = \frac{V_{app}\mu_c}{\epsilon^4 \sigma}, \quad \tilde{p} = \frac{pR_p}{\sigma}, \quad \tilde{\tau}_d = \frac{\tau_d R_p}{\epsilon \sigma}, \quad \tilde{t} = \frac{t\epsilon\sigma}{\mu_d R_p}, \qquad (19)$$

the Eqs. (7)–(8) and (11)–(16) are rendered dimensionless as

$$\frac{\partial \tilde{p}}{\partial \tilde{r}} = \frac{\partial^2 \tilde{v}_r}{\partial \tilde{z}^2}, \qquad \frac{\partial \tilde{p}}{\partial \tilde{z}} = 0 \qquad (20)$$

$$\frac{\partial \tilde{v}_z}{\partial \tilde{z}} + \frac{1}{\tilde{r}}\frac{\partial}{\partial \tilde{r}}(\tilde{r}\tilde{v}_r) = 0 \qquad (21)$$

$$\tilde{v}_r|_{\tilde{z}=\tilde{h}/2} = \tilde{U} \qquad (22)$$

$$\frac{1}{2\lambda^*}\frac{\partial \tilde{h}}{\partial \tilde{t}} = \tilde{v}_z|_{\tilde{z}=\tilde{h}/2} - \frac{1}{2}\frac{\partial \tilde{h}}{\partial \tilde{r}}\, \tilde{v}_r|_{\tilde{z}=\tilde{h}/2} \qquad (23)$$

$$-\frac{\partial \tilde{v}_r}{\partial \tilde{z}}\bigg|_{\tilde{z}=\tilde{h}/2} = \tilde{\tau}_d \qquad (24)$$

$$\tilde{p} = 2 - \frac{1}{2\tilde{r}}\frac{\partial}{\partial \tilde{r}}\left(\tilde{r}\frac{\partial \tilde{h}}{\partial \tilde{r}}\right) + \frac{A^*}{\tilde{h}^3} \qquad (25)$$

$$\tilde{p}|_{\tilde{r}=\tilde{r}_\infty} = 0, \qquad \frac{\partial \tilde{h}}{\partial \tilde{t}}\bigg|_{\tilde{r}=\tilde{r}_\infty} = -\lambda^* \tilde{V}_{app} \qquad (26)$$

and

$$\tilde{h} = \tilde{h}_{00} + \tilde{r}^2 \qquad (27)$$

where $A^* = \frac{A}{6\pi\epsilon^6 R_p^2 \sigma}$ and $\lambda^* = \frac{\mu_d \epsilon}{\mu_c}$. The non-dimensionalized normal stress balance also requires a restriction on the magnitude of the capillary number, $Ca = \frac{\mu_c V_{app}}{\sigma} \approx \epsilon^4$, as discussed for thin film analyses in general by Oron et al. (1997). On the other hand, the boundary integral equation, Eq. (17), becomes

$$\tilde{U} = \frac{1}{\lambda^*} \int_0^{\tilde{r}_\infty} \tilde{I}(\tilde{\rho}, \theta)\, \tilde{\tau}_d\, d\tilde{\rho} = \frac{1}{\lambda^*}\hat{U} \qquad (28)$$

and substituting $r = \tilde{r}$ and $\rho = \tilde{\rho}$ into Eq. (18) gives $\tilde{I}(\tilde{\rho}, \theta)$. Hereafter, all equations are given in dimensionless form; therefore,

tildes are omitted in the transformed variables. Solving Eq. (20), and, applying Eq. (22) at $z = h/2$ together with the symmetry condition at r axis, yields

$$v_r = \frac{1}{2}\frac{\partial p}{\partial r}\left(z^2 - \left(\frac{h}{2}\right)^2\right) + U \qquad (29)$$

clearly indicating two distinct contributions to the radial velocity, the parabolic flow driven by the pressure gradient inside the film and the interfacially-driven plug flow. Then, the tangential component of the stress balance, Eq. (24), becomes

$$-\frac{h}{2}\frac{\partial p}{\partial r} = \tau_d \qquad (30)$$

Once v_r is known, the z component of the film velocity, v_z, is determined via Eq. (21). Finally, by substituting v_z and v_r (given by Eq. (29) into Eq. (23), the thinning equation is found:

$$\frac{\partial h}{\partial t} = \frac{1}{r}\left[\frac{\lambda^*}{12}\frac{\partial}{\partial r}\left(r\frac{\partial p}{\partial r}h^3\right) - \frac{\partial}{\partial r}\left(r\hat{U}h\right)\right] \qquad (31)$$

Despite the differences in the characteristic scales employed, the equation is exactly the same as the Bazhlekov et al. (2000)'s thinning equation, and reveals that the effects of the parabolic and the plug flows in the film are weighted by the dispersed to the continuous phase viscosity ratio via λ^*. That brings out the classification of the interfaces in terms of their mobility. At very high values of λ^*, the interface attains infinitesimal values of $\hat{U}$ and becomes tangentially immobile, whereas at low λ^* the thinning equation is dominated by the plug flow's contribution, earning the title of fully mobile interface following Davis et al. (1989)'s description. In these extreme cases, Eq. (31) can be simplified by only taking into account the dominant terms for the respective case and neglecting the other. Then, for the immobile case

$$\frac{\partial h}{\partial t} = \frac{1}{12\,r}\frac{\partial}{\partial r}\left(r\frac{\partial p}{\partial r}h^3\right) \qquad (32)$$

and for the fully mobile case

$$\frac{\partial h}{\partial t} = -\frac{1}{r}\frac{\partial}{\partial r}\left(r\hat{U}h\right) \qquad (33)$$

can be used as the thinning equation. Notice that, in the immobile case, λ^* is included in the time scale by setting $\tilde{t} = \frac{\mu_c R_p}{\epsilon^2 \sigma}$, which further implies that the right hand side of the velocity boundary condition in Eq. (26) becomes $-V_{app}$. The thinning equation for the fully mobile case, Eq. (33), can be obtained by setting $\lambda^* = 0$ in Eq. (31). Therefore, the fully mobile case is referred to as the $\lambda^* = 0$ case, hereafter. However, this only implies that the first term on the right hand side of Eq. (31) is negligible, and does not suggest the physical value of λ^* to be actually zero. Additionally, even though the name 'the $\lambda^* = 0$ case' used for the fully mobile case evokes the opposite, the λ^* appearing in the boundary condition, Eq. (26), is not zero, but it is rather a small physical value. On the other hand, at moderate values of λ^* (corresponds to Davis et al. (1989)'s partially mobile interface), contributions of both flows have non-negligible effects on thinning and Eq. (31) is directly employed without any further simplifications. In all cases, the thinning equation is coupled with Eq. (25), and except the immobile case, Eqs. (28) and (30) are used to determine $\hat{U}$.

3. Numerical procedure

For each one of the three mobility cases (the partially mobile, the immobile and the fully mobile interfaces) given in Section 2.2, a different solver is employed. However, these solvers share some characteristics: In all cases, the corresponding thinning equation (Eqs. (31), (32) or (33)) is solved simultaneously with Eq. (25). The

boundary conditions given in Eq. (26) hold together with the symmetry conditions for both h and p at $r = 0$. The spatial discretization scheme is either a spectral one based on Chebyshev polynomials, or consists of spectral elements, which are again based on Chebyshev polynomials. The elements are used in some cases to obtain higher spatial resolution without drastically increasing the computational efforts. However, when spectral elements are used, since Chebyshev polynomials are only c_0 continuous on the element boundaries (Patera, 1984; Karniadakis and Sherwin, 2013), the solver fails to give accurate results for differential equations with order higher than one. Therefore, the second order differential equations, the thinning equation (one of Eqs. (31)–(33)) and Eq. (25), are converted into a set of four first order differential equations in the spectral element solvers. The transformation is done by setting $Y_1 = h$, $Y_2 = \frac{\partial h}{\partial r}$, $Y_3 = p$, $Y_4 = \frac{\partial p}{\partial r}$. In all solvers, the second order backward differentiation is used to discretize the time derivatives.

In mobile cases, computation of $\hat{U}$ is required via the Boundary Integral equation, Eq. (28). However, the equation has an inherent singularity at $\rho = r$ and $\theta = 0$ as can be seen from Eqs. (17) to (18). To the best of our knowledge, the works in the literature that simulate similar thinning equations to ours, do not explicitly reveal their methods of coping with the singularity. Therefore, we attempt to give some insight on our method in this section. First, starting with Eq. (28), the integral defining $\hat{U}$ is divided into three parts to isolate the singularity:

$$\hat{U} = \int_0^{r_\infty} I(\rho, \theta) \, \tau_d \, d\rho = \int_0^{r-\delta} I(\rho, \theta) \, \tau_d \, d\rho$$
$$+ \int_{r-\delta}^{r+\delta} I(\rho, \theta) \, \tau_d \, d\rho + \int_{r+\delta}^{r_\infty} I(\rho, \theta) \, \tau_d \, d\rho \tag{34}$$

where δ is a small arbitrary number. Here, the singularity is isolated in the second term on the right hand side of Eq. (34), enabling efficient and accurate computation of the first and the last terms. The kernels in these terms, $I(\rho, \theta)$, are merely geometric functions, and as a result, computed only once at the beginning of the computation. The singular integral, however, is treated further. Following Section 8.2 of Scott et al. (2013), a coordinate transformation (sketched in Fig. 2) is applied to shift the singular point to the origin of a polar coordinate system, from (ρ, θ) to (R, φ) via

$$\rho - r = R \sin\varphi, \qquad \theta = R \cos\varphi \tag{35}$$

As can be seen from Fig. 2, the transformation requires the integration domain to be handled in three separate parts. The singular integral, then, is written in terms of the summation of these three integrals as

$$\int_{r-\delta}^{r+\delta} I(\rho, \theta) \tau_d(\rho) \, d\rho$$
$$= \sum_{k=1}^{3} \left\{ \int_0^{R_k} \int_{\varphi_k}^{\varphi_{k+1}} I(R, \varphi) \tau_d(R, \varphi) R \, d\varphi \, dR \right\} \tag{36}$$

where

$$R_k = \left[\frac{-\delta}{\sin\varphi}, \frac{\pi}{\cos\varphi}, \frac{\delta}{\sin\varphi} \right], \qquad \varphi_k = \left[\frac{-\pi}{2}, tan^{-1}\left(\frac{-\delta}{\pi} \right),$$
$$tan^{-1}\left(\frac{\delta}{\pi} \right), \frac{\pi}{2} \right]$$

and

$$I(R, \varphi) = \frac{(r + R\sin\varphi)\cos(R\cos\varphi)}{\sqrt{r^2 + (r + R\sin\varphi)^2 - 2r(r + R\sin\varphi)\cos(R\cos\varphi)}} \tag{37}$$

Next, by assuming τ_d is constant in the δ vicinity of $r = \rho$, Eq. (34) turns out to be

$$\hat{U} = \int_0^{r-\delta} I(\rho, \theta) \, \tau_d \, d\rho + \tau_d \sum_{k=1}^{3} \left\{ \int_0^{R_k} \int_{\varphi_k}^{\varphi_{k+1}} I(R, \varphi) R \, d\varphi \, dR \right\}$$
$$+ \int_{r+\delta}^{r_\infty} I(\rho, \theta) \, \tau_d \, d\rho \tag{38}$$

in which, now, the singular part of the integral is also given as a purely geometrical function, that is computed only once throughout the simulation. Finally, all the integrals, in Eq. (38), are transformed into matrix form using quadrature rules, so that the Boundary Integral equation can be written as

$$\hat{U} = [A]\tau_d \tag{39}$$

where $[A]$ is the integration matrix. Some key details in derivation of $[A]$ is provided in the Appendix A. The accuracy of the approximation might depend heavily on the value of the small parameter δ when it is selected poorly. In our simulations this value is taken as low as 10^{-4} - 10^{-5}, around which no further significant dependence of $\hat{U}$ on the value of δ is observed. For mobile cases (except for $\lambda^* = 0$), first, the Eqs. (25) and (31) are solved simultaneously at a given time step; then, through Eqs. (30) and (39), τ_d and $\hat{U}$ are determined; and finally, $\hat{U}$ is fed to the next time step as an input. Whereas, in the fully mobile case ($\lambda^* = 0$), Eqs. (25), (30), (33) and (39) are solved simultaneously to obtain a more stable numerical scheme, which is found to be a must, especially in the early stages of the simulation.

4. Results and discussion

Although the models in this work are not capable of rendering the rupture of the interface, it is possible to foresee it by considering non-zero A^* values. At a critical film thickness that depends on the magnitude of A^*, the attractive van der Waals forces become much more influential than the resistance within the film. This results in very rapid thinning of the film, after which the rupture of the interface is extremely likely. Since the time scale of the rupture is much smaller than the time scale of the film drainage until the critical rupture thickness is reached, the coalescence time is determined by approximating it as the drainage time, without actually modeling the rupturing phenomenon itself. Due to this approach, the value given as the dimensionless coalescence time, t_c, is the simulation time between the beginning of the numerical simulation and the time right before the rupture in the corresponding simulation.

4.1. Immobile interfaces

In their Fig. 4, Klaseboer et al. (2000) presents the film thickness profiles at different times obtained for their immobile model with the constant approach velocity boundary condition. To validate the immobile solver described in Section 3, their results are reproduced by setting $A^* = 0$ and $V_{app} = 1$, and given in Fig. 3. The results of our immobile solver seem to be in perfect agreement with those of Klaseboer et al. (2000)'s. For $t > 0$, the formation of the dimple is clearly seen in Fig. 3. However, due to the absence of the disjoining pressure ($A^* = 0$), the rupture of the film is not estimated.

Fig. 4 presents the coalescence time, t_c, as a function of the relative approach velocity for different non-zero values of A^*. For all the values of A^* considered here, three distinct types of drainage/coalescence behavior are observed. First, at very low approach velocities, t_c decreases with V_{app} following a power law type relation, i.e., a linear relation between $\log(t_c)$ and $\log(V_{app})$. An example of the 'low velocity drainage' can be seen in Fig. 5(a),
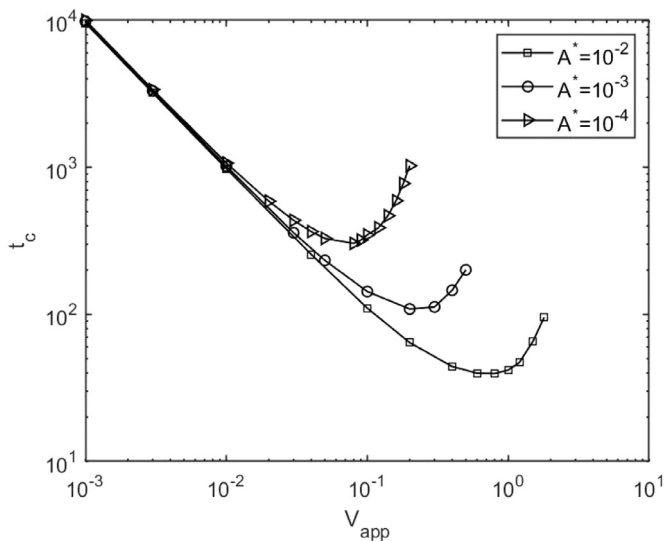
Fig. 4. Coalescence time for immobile interfaces as a function of the relative approach velocity. Profiles are obtained with $h_{00} = 10$ and $r_\infty = 15$.

in which the time evolution of the film thickness for $V_{app} = 0.003$ and $A^* = 10^{-4}$ is shown. In that type of drainage, the attractive van der Waals forces become significant before the capillary forces act substantially, resulting in rupture at $r = 0$, the center of the fluid particle (nose rupture). The low velocity drainage behavior continues until a critical velocity is reached. After this critical velocity, the capillary forces become influential before the rupture

occurs, and as a result, a dimple shape emerges. Hereafter, this critical velocity is referred to as the dimpling velocity, V_{dimp}. The results indicate that V_{dimp} increases as the attractive forces gets stronger meaning that stronger capillary forces are required for the dimple formation as A^* increases. Fig. 5(b) reveals the typical drainage process (obtained for $V_{app} = 0.01$ and $A^* = 10^{-4}$) in this regime. Although, first two profiles are similar to the ones observed in the low velocity drainage regime, in later stages of the drainage (after $t > 1040$) the dimple becomes visible, and the rupture occurs on the rim instead of the center (rim rupture). In this regime, t_c continues to decrease with increasing V_{app}, but the decrease becomes less and less dramatical as V_{app} increases, and eventually, t_c passes through a minimum. Right after the minimum, further increase in the velocity brings out the third regime, where multiple rim-like structures emerge before rupture and t_c increases with V_{app}. This second critical velocity is denoted as V_{mult}. Two examples of the time evolution of the film thickness in the 'multiple-rim' regime are provided in Fig. 5(c) and (d), which fall into the category of pimpling and rippling of the interface, respectively. Here, the pimple refers to the emergence of an additional local minimum such that the main rim is positioned in between the center of the fluid particle and the new local minimum, whereas the term ripple is used when multiple additional minima and maxima are encountered (Reader may refer to Section 3.1.2 of Chan et al. (2011) for more detail and visualization of the interface shapes). The slope of $\log(V_{app})$ versus $\log(t_c)$ in the first region, and the critical velocities, V_{dimp} and V_{mult}, can be used to identify each curve in Fig. 4. The corresponding values are determined as: $d(\log(t_c))/d(\log(V_{app})) = [-0.994, -0.992, -0.988]$, $V_{dimp} = [0.2, 0.05, 0.01]$ and $V_{mult} = [0.9, 0.3, 0.09]$, for $A^* = $
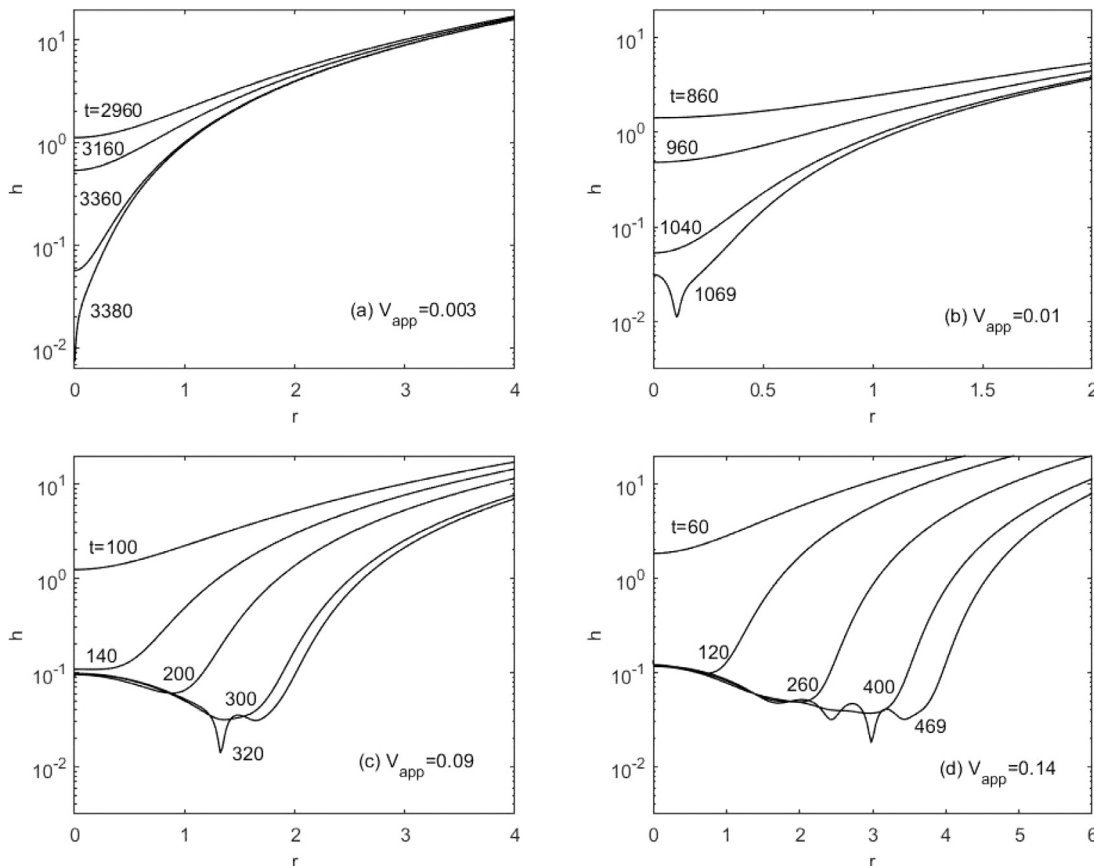

Fig. 5. Time evolution of the film thickness in different regimes: (a) the low velocity regime, the nose rupture, (b) the dimpled drainage regime, the rim rupture, (c) and (d) the multiple rim regime (pimpling and rippling behaviors, respectively). Profiles are obtained with $A^* = 10^{-4}$, $h_{00} = 10$ and $r_\infty = 15$.
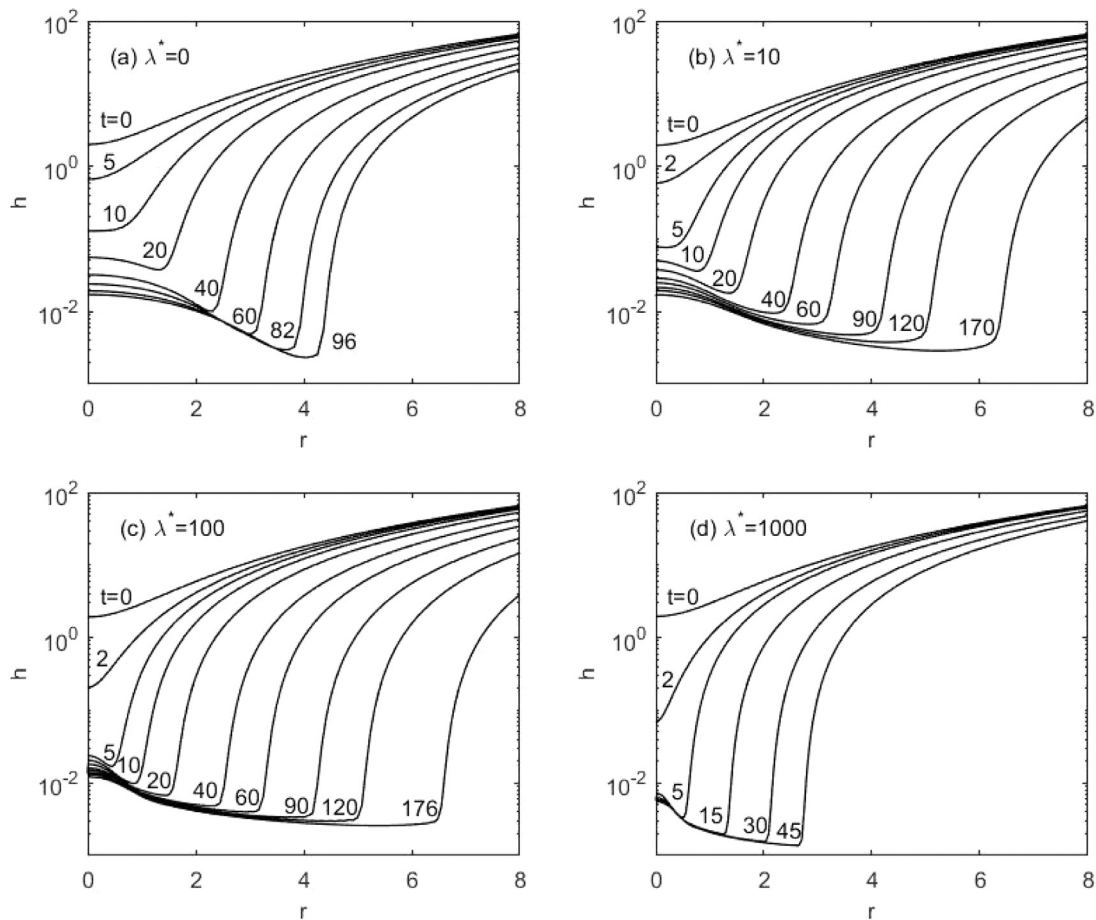
Fig. 6. Fig. 4 of Bazhlekov et al. (2000) reproduced for validation of the mobile solvers. Thin film thickness as a function of r and t for (a) $\lambda^* = 0$, (b) $\lambda^* = 10$, (c) $\lambda^* = 100$ and (d) $\lambda^* = 1000$. In all cases $A^* = 0$, $\lambda^* V_{app} = 1$, $h_{00} = 2$ and $r_\infty = 30$.

$[10^{-2}, 10^{-3}, 10^{-4}]$, implying that, just as V_{app} does, V_{mult} also increases with increasing A^*, whereas the slope decreases. The analysis is carried out by assuming that the interface immobility is due to the very high dispersed to continuous phase viscosity ratio, however the applicability of the observations should be independent of the source of the interfacial immobilization, as in all types of immobilization the tangential velocity of the interface, $\hat{U}$, is zero.

4.2. Mobile interfaces

To validate the mobile solvers described in Section 3, the results of Bazhlekov et al. (2000) for the constant approach velocity boundary condition are reproduced by setting $A^* = 0$ and $\lambda^* V_{app} = 1$. Fig. 6 corresponds to their Fig. 4 and presents the evolution of the film thickness as a function of time and radial position at different λ^*. For all values of λ^* presented in the Fig. 6 dimple formation at the interface is observed. Although it is not possible to compare the numerical values for the film thickness directly, excellent visual agreement is observed for partially mobile cases $\lambda^* = 10$, $\lambda^* = 100$ and $\lambda^* = 1000$. For $\lambda^* = 0$, however, our solver does not produce the very sharp gradients shown by Bazhlekov et al. (2000) at $t = 96$, although at the earlier times the results seem to be in agreement. This discrepancy might appear due to the different numerical techniques employed, i.e., finite difference in Bazhlekov et al. (2000) and spectral methods in this work, or due to the differences in treatment of the boundary integral. Here, we cannot give any further discussion on the latter

possibility, since Bazhlekov et al. (2000) does not provide any detailed information on their treatment.

As mentioned earlier in the end of Section 2.2, the $\lambda^* = 0$ case refers to the fully mobile interfaces. In this case, the value of λ^* is sufficiently small (yet non-zero) enough to render the first term on the right hand side of Eq. (31) negligible, enabling us to approximate the drainage via Eq. (33) by setting $\lambda^* = 0$ in Eq. (31). However, in the boundary condition, Eq. (26), λ^* is not taken as zero, but rather as the small physical value itself, implying that $\lambda^* V_{app} \neq 0$. Then, a viscosity ratio sweep is carried out to determine the λ^* value, below which the drainage can be approximated with the $\lambda^* = 0$ case. To carry out the viscosity ratio sweep, first, the results for the very low viscosity ratio limit are obtained by solving the $\lambda^* = 0$ case for each value of the non-dimensionalized Hamaker constant, $A^* = [10^{-2}, 10^{-3}, 10^{-4}]$. Then, starting with $\lambda^* = 100$, the viscosity ratio is lowered to one tenth of its previous value, until the results visually converge to the results of $\lambda^* = 0$, i.e., the low viscosity ratio limit. For $A^* = 10^{-2}$ and $A^* = 10^{-3}$, this value is found as $\lambda^* = 0.1$, whereas for $A^* = 10^{-4}$, $\lambda^* = 1$ seems sufficiently close. For any phyiscal value of λ^* smaller than each corresponding limit, the results from the $\lambda^* = 0$ case can be used to estimate the drainage/coalescence behavior.

The left column of Fig. 7 reveals the behavior of t_c as a function of $\lambda^* V_{app}$, and the actual V_{app} dependence of t_c is presented on the right column by dividing each dataset by the corresponding value of λ^*. On the right column, the $\lambda^* = 0$ results are not given, since it implies a division by zero. However, the curves given on the left column for $\lambda^* = 0$ can be adjusted by dividing $\lambda^* V_{app}$ by the small physical value of λ^*. The only restriction is that this physical
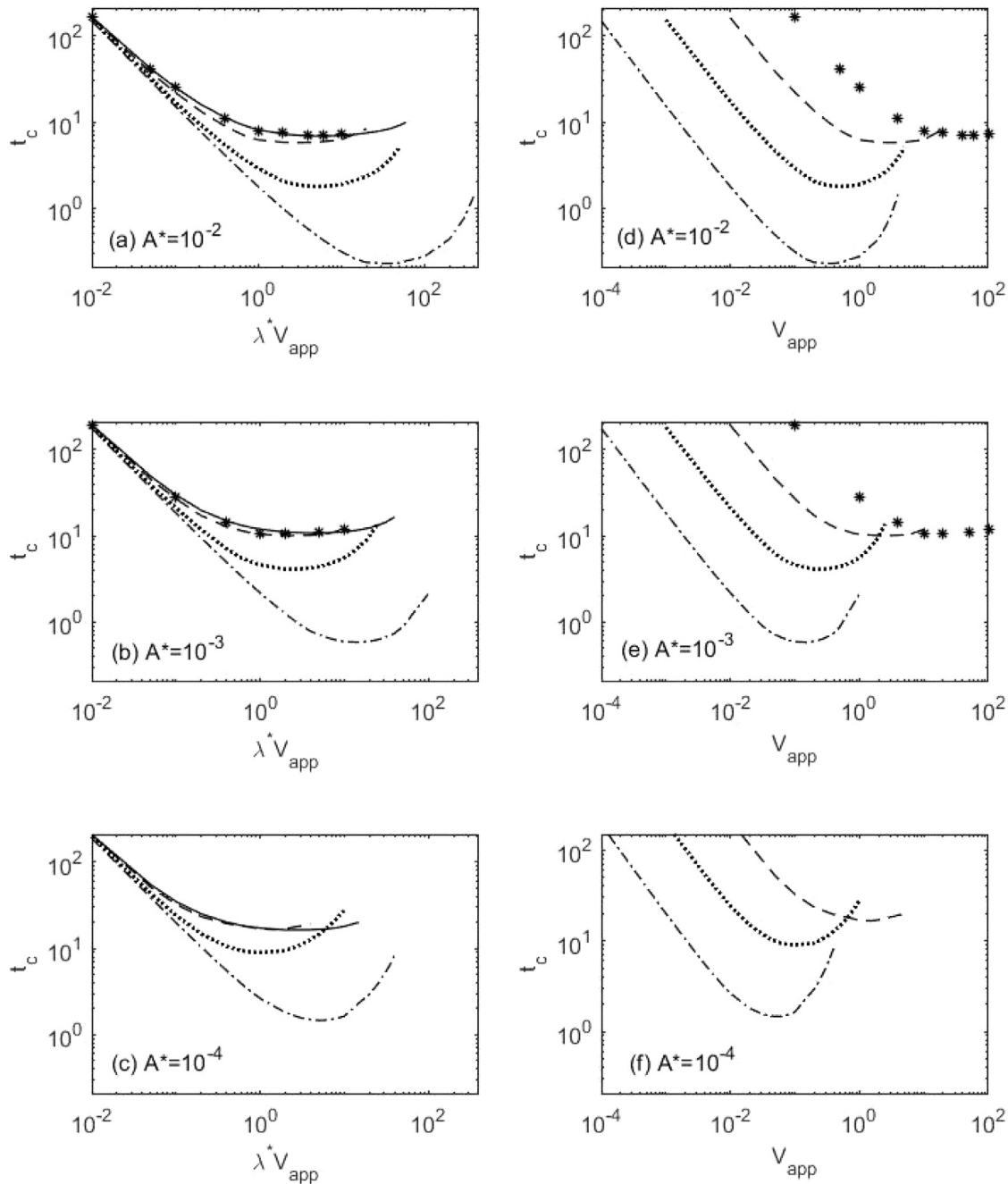
Fig. 7. Coalescence time for mobile interfaces as a function of $\lambda^* V_{app}$ on the left, (a) - (c), and as a function of V_{app} on right, (d) - (f). Each curve corresponds to a different λ^* value: solid line ($\lambda^* = 0$), stars ($\lambda^* = 0.1$), dashed line ($\lambda^* = 1$), dotted line ($\lambda^* = 10$), dashed-dotted line ($\lambda^* = 100$). All results are obtained with $h_{00} = 2$ and $r_\infty = 30$.

value should be smaller than 0.1 for $A^* = 10^{-2}$ and $A^* = 10^{-3}$, and smaller than 1 for $A^* = 10^{-4}$ based on the insight obtained from the viscosity ratio sweeps mentioned earlier in this section. This implies that the changes in λ^* in that limit do not actually affect the behavior of t_c against V_{app}, but rather only shifts the values of V_{app}.

Similar to the mobile interfaces, three distinct types of behavior are also observed for the immobile interfaces: the linear slow drainage region for low velocities, the dimpled drainage region after V_{dimp} is achieved, and after passing a minimum the multiple-rim region where t_c begins to increase with V_{app}. The linear regime has also been observed experimentally by Orvalho et al. (2015). Furthermore, the regime implies that as V_{app} approaches zero, t_c attains very large values. This observation coincides with the ex-

perimental results of Yaminsky et al. (2010), where they observe a stable film in finite time in the very small V_{app} limit. Both the first and second regimes, as well as the minimum point, have been observed experimentally by Del Castillo et al. (2011). However, to the best of our knowledge, an experimental work that could be used to validate the multiple-rim region does not exist in the literature. The right column of Fig. 7 shows that at a given value of V_{app}, t_c is larger for smaller λ^* as long as V_{app} falls into the linear or the dimpled drainage regions for both values of λ^* compared, or in other words as long as multiple-rims are not present in neither of the λ^* values. On the other hand, as can be concluded from the presence of intersecting curves in the multiple-rim regime (e.g. $\lambda^* = 1$ and $\lambda^* = 10$ curves in Fig. 7 (f)), t_c can be larger for higher λ^*. As an increase in λ^* can be analyzed as a decrease in the continuous phase
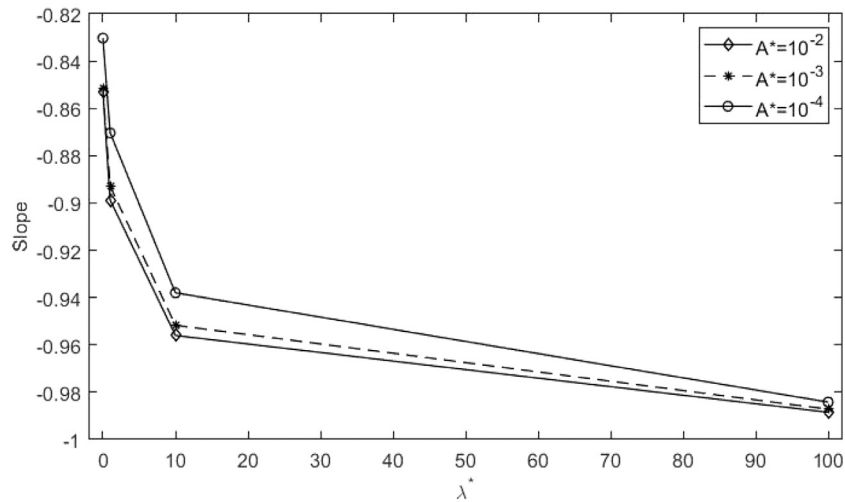
Fig. 8. The slope, $d(\log(t_c))/d(\log(V_{app}))$, in the slow drainage regime computed at different A^* for $\lambda^* = 0, 1, 10, 100$.
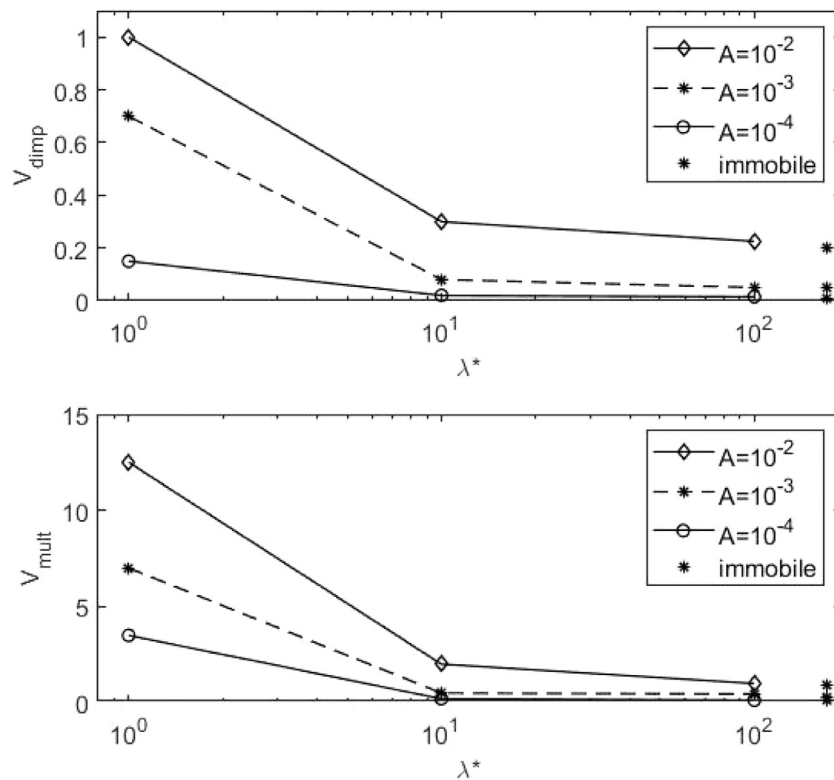

Fig. 9. Critical velocities restricting the dimpled drainage region, V_{dimp} and V_{mult}, computed at different A^* for $\lambda^* = 1, 10, 100$. The values given for immobile interfaces ($\lambda^* \to \infty$) do not correspond to any particular value of λ^* and positioned on the far right of the plots only for the purpose of visual comparison between the critical velocities.

viscosity, higher film drainage rates (and as a results lower t_c) for higher λ^* are expected. This behavior is clearly observed for the first two regions. However, the possible opposite trend in the third region might be explained by the emergence of multiple-rims, as the emergence of rims is shown to slow down the drainage and consequently increase t_c. In addition, Del Castillo et al. (2011) observes an almost constant t_c after the minimum point instead of the obvious increase in the present results, and does not report any multiple-rim shape. This deficiency as V_{app} increases drastically may suggest that the drainage transforms into an inertial one meaning that it is governed by the acceleration of the particles, which is not adequately modeled by the drainage equations em-

ployed in this work, rather than being governed by the viscous effects in the film or the interfacial deformations.

In the first region, the slow drainage regime, the attractive van der Waals forces are dominant compared to the capillary forces. That results in no dimpling and the rupture is on the center of the particle, i.e., the nose type rupture is observed. Here, $\log(t_c)$ is a linear function of $\log(V_{app})$. As can be seen from Fig. 8, the slope of this linear relation, $d(\log(t_c))/d(\log(V_{app}))$, varies with A^* and λ^*. In the low viscosity ratio limit, i.e., $\lambda^* = 0$ solution, the respective slopes for $A^* = [10^{-2}, 10^{-3}, 10^{-4}]$ are determined as -0.853, -0.852 and -0.830, which show an exceptional agreement with the experimentally determined value of -0.85 by

Orvalho et al. (2015) in their experiments with bubbles in liquids of different viscosities. On the other extreme, $\lambda^* \to \infty$, the values of the slopes seem to approach those obtained for the immobile interfaces in Section 4.1, -0.994, -0.992 and -0.988 for $A^* = [10^{-2}, 10^{-3}, 10^{-4}]$, respectively.

The dimpled drainage regime, follows the slow drainage region. Here, with the help of the increasing V_{app}, the capillary forces manage to act significantly before the coalescence, resulting in dimpling of the interface. The interface ruptures at the rim instead of at the center of the particle. The coalescence time still decreases with V_{app}, but less dramatically compared to the first region, until it eventually reaches to a minimum. This region is observed for $V_{dimp} < V_{app} < V_{mult}$. The critical velocities, V_{dimp} and V_{mult} for different values of A^* and λ^* are presented in Fig. 9, with the stars at the right end standing for the immobile solver's results, which can be analyzed as the values for $\lambda^* \to \infty$. As discussed for the immobile interfaces, the critical velocities again decrease with decreasing A^*. Now, in addition, the effect of λ^* on V_{dimp} and V_{mult} are revealed: in all cases, they decrease with increasing λ^* and eventually converge to the values obtained for immobile interfaces. Again, the increase in λ^* can be interpreted as a decrease in the film viscosity. As the film viscosity decreases, the film is expected to show less resistance both to the drainage and to the emergence of the rims on the interface. Therefore, for higher λ^*, lower approach velocities are expected to be required to overcome the resistance from the film against the emergence of rims, which results in lower critical velocities, V_{dimp} and V_{mult}. The critical velocities for the $\lambda^* = 0$ case are not given in Fig. 9, once again to avoid division by 0. However, the $\lambda^* V_{app}$ values separating the regions are

found to be $\lambda^* V_{dimp} = [0.4, 0.1, 0.05]$ and $\lambda^* V_{mult} = [17, 25, 30]$ for $A^* = [10^{-2}, 10^{-3}, 10^{-4}]$, respectively. In the limit of $\lambda^* \to 0$, these values can be converted into V_{dimp} and V_{mult} values by dividing them by the physical value of λ^*.

Previously, for the immobile interfaces, the increase in t_c in the last region has been associated with the emergence of the additional rims at the interface. This observation still holds for all the cases where $\lambda^* \neq 0$. However, when $\lambda^* = 0$ in the drainage equation, the interface begins to exhibit a wimple shape after V_{mult} is achieved, instead of pimpling. Just like the pimple or the ripple shapes, the wimple still leads to an increase in the surface area and in t_c. Fig. 10 (a) and (b) demonstrate pimpling and wimpling of the interface, respectively. As can be seen in the case of the pimple, a secondary local minimum appears after the rim and dh/dr between the center and the rim is negative. On the other hand, in the case of the wimple, a local maximum appears in between the rim and the center, and dh/dr is positive between center and the local maximum. In all cases where $\lambda^* \neq 0$ given in this work, no wimpled interface is observed. This observation implies that the existence of the pressure gradient term in the drainage equation Eq. (31), i.e., the parabolic component of the film velocity, favors the pimpling or rippling of the interface and prohibits the emergence of a wimple shape.

5. Conclusions

In this work, the effect of the relative approach velocity (V_{app}) together with the effects of the dispersed to continuous phase viscosity ratio (via λ^*) and the attractive Van der waals forces (via A^*) on the coalescence time of two fluid particles colliding along their centerlines (t_c), is investigated. Although models similar to the ones used in the current work are present in the literature, the preexisting ones fail to estimate the coalescence time since they do not include the disjoining pressure in their models. Furthermore, they fail to investigate the effect of the approach velocity explicitly on the drainage rate and consequently on the coalescence time. The modifications on the models present in the current study enable the investigation of t_c as a function of V_{app}, λ^* and A^*, thereby matching some experimental observations such as those of Yaminsky et al. (2010), Del Castillo et al. (2011) and Orvalho et al. (2015).

The simulations indicate that regardless of the magnitudes of the viscosity ratio and the attractive Van der Waals forces, three distinct behaviors of drainage/coalescence are observed as V_{app} changes. In other words, for all values of λ^* and A^*, as V_{app} increases the sequential regimes of the linear slow drainage, the dimpled drainage and the multiple-rim drainage are observed. To quantify the behavior of the coalescence time the critical velocities separating the regimes, V_{dimp} and V_{mult}, and the slope of $d(\log(t_c))/d(\log(V_{app}))$ in the first region are computed. V_{dimp} corresponds to V_{app} at which the interface dimples and the linear trend between $\log(t_c)$ and $\log(V_{app})$ disappears, whereas V_{mult} is the value of V_{app} at which multiple-rims begin to emerge and t_c obtains its minimum value. The slope of the linear region decreases with increasing A^* for all values of λ^* including the immobile interfaces where $\lambda^* \to \infty$. Similarly, for all values of A^*, increasing λ^* results in a decrease in the slope, which converges to -0.99 and -0.85 in the limits of $\lambda^* \to \infty$ and $\lambda^* \to 0$, respectively. The critical velocities, V_{dimp} and V_{mult}, decrease with increasing λ^* and decreasing A^*, and eventually converge to the corresponding values obtained via the immobile solver ($\lambda^* \to \infty$). The former behavior is associated to the lower resistance to the emergence of rims on the interface at higher values of λ^*, i.e., smaller velocities are sufficient to overcome the resistance in the film against the formation of the rims. On the other hand, the latter is explained by the requirement of the lower velocities for the capillary forces to
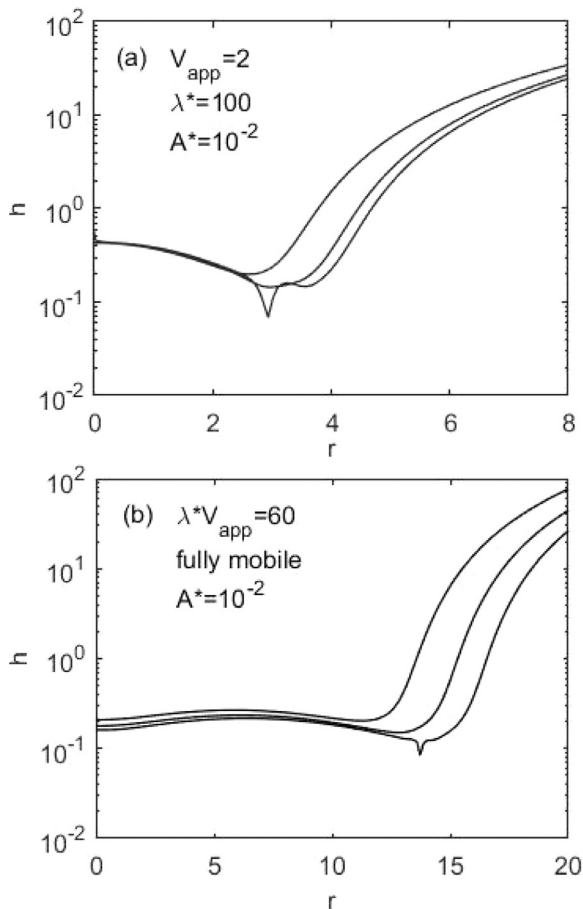

Fig. 10. Time evolution of the film thickness for (a) the pimple and (b) the wimple interface shapes. All results are obtained with $h_{00} = 2$ and $r_\infty = 30$.

dominate over the weaker attractive van der Waals forces, which again favor the emergence of rims on the interface. Finally, in the third region, the interface pimples first and ripples afterwards as V_{app} further increases when $\lambda^* \neq 0$, whereas wimpling of the interface is encountered instead of pimpling in the $\lambda^* = 0$ case. This suggests that the presence of the parabolic contribution in the film velocity favors the pimpling of the interface rather than wimpling.

The conclusions derived from the current work coincide with a number of experimental observations present in the literature. The trends observed in the linear and the dimpled regions, together with the presence of a minimum, qualitatively agree with the results of Del Castillo et al. (2011) obtained in their experiments with air bubbles in pure water. Moreover, in the limit of $V_{app} \rightarrow 0$, the simulations suggest an infinite time is required for coalescence to occur, which agree with the Yaminsky et al. (2010)'s experimental observation. A quantitative agreement is also present between the slopes of the first region obtained via the simulations in the limit of very low viscosity ratios, i.e., $\lambda^* \rightarrow 0$, and the slope of the linear trend obtained by Orvalho et al. (2015) in their experiments with air bubbles and liquids with various viscosities. The experimental value determined by Orvalho et al. (2015) reads $d(\log(t_c))/d(\log(V_{app})) = -0.85$, whereas our simulations determines $d(\log(t_c))/d(\log(V_{app})) = [-0.853, -0852, -0.830]$ for $A^* = [10^{-2}, 10^{-3}, 10^{-4}]$. The lack of experimental validation of the third region present in our simulations may indicate our models' low accuracy in the high V_{app} limit due to additional physical mechanisms missing in the models, which might be only non-negligible for high V_{app}. For further quantitative comparison between t_c values obtained in the present work and the ones reported in the experimental studies, the value of the small parameter, ϵ, is needed. The determination of ϵ requires the knowledge of the particle size and the initial separation distance, at which the fluid particles start to interact, as it can be computed through Eq. (5). Unfortunately, the experimental studies mentioned here do not provide clear information on the initial separation distance. Once ϵ is known, the values of V_{app}, A^* and λ^* that coincide with the experimental parameters can be computed, and the corresponding t_c can be read from either Fig. 4 or Fig. 7. Finally, by employing the time scale given in Eq. (19), the dimensionless t_c value can be dimensionalized to reveal the actual time of coalescence.

Acknowledgments

Appendix

First, the geometric function $I(\rho, \theta)$ given by Eq. (18) computed using MATLAB's built-in integration subroutines. In that step, the value of $I(\rho, \theta)$ at the singular points, i.e., $\rho = r$, is approximated as the average of $I(\rho, \theta)$ evaluated at $\rho = r - \delta$ and $\rho = r + \delta$. The averaged integrand is denoted as $I_{av}(\rho, \theta)$, hereafter. That enables the computation of the non-singular integrals, the first and third ones in Eq. (38), as a single continuous integral. However, this approach results in a small region in between $\rho = r - \delta$ and $\rho = r + \delta$, which is taken into account by both the new non-singular integral and the singular integral in Eq. (38). Then, it is possible to rewrite Eq. (38) as

$$\hat{U}(r) = \int_0^{r_\infty} I_{av}(\rho, \theta)\, \tau_d \, d\rho + \tau_d \sum_{k=1}^{3} \left\{ \int_0^{R_k} \int_{\varphi_k}^{\varphi_{k+1}} I(R, \varphi) R \, d\varphi \, dR \right\} + E(r) \tag{40}$$

where E emerges due to the double-counting of the small region. Once the integration with respect to θ is carried out in $I_{av}(\rho, \theta)$,

the θ dependence disappears and a kernel $Z(r, \rho)$ that multiplies the stress τ_d appears. Then, Eq. (40) becomes

$$\hat{U}(r) = \int_0^{r_\infty} Z(\rho, r)\, \tau_d \, d\rho + \tau_d \sum_{k=1}^{3} \left\{ \int_0^{R_k} \int_{\varphi_k}^{\varphi_{k+1}} I(R, \varphi) R \, d\varphi \, dR \right\} + E(r) \tag{41}$$

Following Guo et al. (2013) the definite integration of a quantity v can be carried out by using the collocation points (n) via

$$\int_{-1}^{1} v d\rho = - \sum_{even, n=0}^{N} \frac{2\hat{v}_n}{n^2 - 1} \tag{42}$$

where v and its counterpart in Chebyshev pseudospecturm, $\hat{v}$, is related via

$$T^{-1} v = \hat{v} \tag{43}$$

and

$$\left(T^{-1}\right)_{np} = \frac{2(-1)^n}{N \bar{c}_n \bar{c}_p} \cos\left(np\frac{\Pi}{N}\right) \tag{44}$$

where $\bar{c}_n = 2$ for $n = 0$ or $n = N$, and $\bar{c}_n = 1$ for $1 \leq n \leq N - 1$. Here, the integrand v corresponds to $Z(\rho, r)\tau_d$ for the first integral in Eq. (41). Then, by substituting $\hat{v}$ via Eq. (43)

$$\int_{-1}^{1} v d\rho = - \sum_{even, n=0}^{N} \frac{2\hat{v}_n}{n^2 - 1} = - \sum_{even, n=0}^{N} \frac{2\left(T^{-1} v\right)_n}{n^2 - 1} \tag{45}$$

is obtained, where T^{-1} is known in matrix form as given by Eq. (44). This further implies that the right hand side of Eq. (45) can be rewritten as

$$\int_{-1}^{1} v d\rho = - \sum_{even, n=0}^{N} \frac{2\left(T^{-1} v\right)_n}{n^2 - 1} = bv \tag{46}$$

where b is a known row vector, which multiplies the column vector v to give the result of the integration. Finally, by mapping the integration domain defined in $[-1, 1]$ to the domain of interest $[0, r_\infty]$

$$\int_0^{r_\infty} v d\rho = \tilde{b}v \tag{47}$$

relation is obtained. Here, $\tilde{b}$ is scaled due to the mapping of the integration domain. That operation corresponds to a single integration with respect to ρ at a given r. It is possible to compose a matrix $[\tilde{B}]$, which carries out the integration with respect to ρ for all r. This approach is proven to be accurate by testing the matrix against various analytically integrable functions. Then, Eq. (41) can be written as

$$\hat{U}(r) = [\tilde{B}]Z(\rho, r)\tau_d + \tau_d \sum_{k=1}^{3} \left\{ \int_0^{R_k} \int_{\varphi_k}^{\varphi_{k+1}} I(R, \varphi) R \, d\varphi \, dR \right\} + E(r) \tag{48}$$

in which the non-singular part of $\hat{U}$ is given in terms of an integration matrix $[\tilde{B}]$ applying on $Z(\rho, r)\tau_d$. Since $Z(\rho, r)$ is known, $[C_1(\rho, r)] = [\tilde{B}]Z(\rho, r)$ is defined in order to write down the equation in a more compact form. Next, the integrals in the second term of Eq. (41) are computed once again using the built-in integration functions of MATLAB and summed, yielding the multipliers of τ_d in that term, which is denoted as $[C_2]$. Here, $[C_2]$ is a function of ρ and r, but it is a diagonal matrix, since this part of the integral corresponds to the singular part, i.e., defined for $\rho = r$. Then, Eq. (48) becomes

$$\hat{U}(r) = [C_1(\rho, r)]\tau_d + [C_2(\rho, r)]\tau_d + E(r) \tag{49}$$

After all the manipulations, only $E(r)$ remains to be dealt with. This area that has been taken into twice corresponds to the area of the

trapezoidal area under $Z(\rho, r)\tau_d$ between $\rho = [r - \delta, r + \delta]$, which has to be subtracted from $\hat{U}$. The area of the trapezoid is given by

$$Area = \frac{\left| (Z(\rho, r)\tau_d)|_{\rho=r+\delta} - (Z(\rho, r)\tau_d)|_{\rho=r-\delta} \right|}{2} 2\delta \qquad (50)$$

Since δ is a very small number, $\tau_d(r - \delta) \approx \tau_d(r) \approx \tau_d(r + \delta)$ is a valid approximation. Based on this approximation and since τ_d is always positive in the physical system of the interest, Eq. (50) can be written as

$$Area = \frac{\left| Z(\rho, r)|_{\rho=r+\delta} - Z(\rho, r)|_{\rho=r-\delta} \right|}{2} 2\delta \, \tau_d \qquad (51)$$

Furthermore, due to the averaging procedure carried out in the beginning of the treatment, $Z(r - \delta, r)$ and $Z(r + \delta, r)$ are known. Then, the coinciding area for each point can be written as the product of a diagonal matrix $-[C_3]$ and τ_d via Eq. (51). Since, the area has to be subtracted $[C_3]\tau_d$ corresponds to $E(r)$ of Eq. (49). Then,

$$\hat{U}(r) = [C_1(\rho, r)]\tau_d + [C_2(\rho, r)]\tau_d + [C_3(\rho, r)]\tau_d = [A(\rho, r)]\tau_d \qquad (52)$$

where $[A]$ is the Boundary Integral integration matrix in Section 3. Provided that the collocation points are fixed throughout the simulation, $[A]$ appears to be purely geometrical meaning that it is computed only once at the beginning of the simulation. The decoupling of $[A]$ and τ_d, therefore, significantly lowers the computational effort. Expressing the Boundary Integral equation in matrix form also proven to be useful as it enables the implicit implementation of Eq. (28) to the solver via Eq. (39).

References

Abid, S., Chesters, A.K., 1994. The drainage and rupture of partially-mobile films between colliding drops at constant approach velocity. Int. J. Multiphase Flow 20 (3), 613–629.

Bazhlekov, I.B., Chesters, A.K., Van de Vosse, F.N., 2000. The effect of the dispersed to continuous-phase viscosity ratio on film drainage between interacting drops. Int. J. Multiphase Flow 26 (3), 445–466.

Chan, D.Y., Klaseboer, E., Manica, R., 2011. Film drainage and coalescence between deformable drops and bubbles. Soft Matter 7 (6), 2235–2264.

Chesters, A., 1991. Modelling of coalescence processes in fluid-liquid dispersions: a review of current understanding. Chem. Eng. Res. Des. 69 (A4), 259–270.

Chesters, A.K., Hofman, G., 1982. Bubble coalescence in pure liquids. In: In Mechanics and Physics of Bubbles in Liquids. Springer, Dordrecht, pp. 353–361.

Coulaloglou, C.A., 1975. Dispersed phase interactions in an agitated flow vessel. Illinois Institute of Technology, Chicago Ph.D. thesis. Ph.D. Dissertation.

Davis, R.H., Schonberg, J.A., Rallison, J.M., 1989. The lubrication force between two viscous drops. Phys. Fluids A 1 (1), 77–81.

Del Castillo, L.A., Ohnishi, S., Horn, R.G., 2011. Inhibition of bubble coalescence: effects of salt concentration and speed of approach. J. Colloid Interface Sci. 356 (1), 316–324.

Guo, W., Labrosse, G., Narayanan, R., 2013. The Application of the Chebyshev-Spectral Method in Transport Phenomena. Springer Science & Business Media.

Horn, R.G., Del Castillo, L.A., Ohnishi, S., 2011. Coalescence map for bubbles in surfactant-free aqueous electrolyte solutions. Adv. Colloid Interface Sci. 168 (1–2), 85–92.

Howarth, W.J., 1964. Coalescence of drops in a turbulent flow field. Chem. Eng. Sci. 19 (1), 33–38.

Karniadakis, G., Sherwin, S., 2013. Spectral/hp Element Methods for Computational Fluid Dynamics. Oxford University Press.

Kirkpatrick, R.D., Lockett, M.J., 1974. The influence of approach velocity on bubble coalescence. Chem. Eng. Sci. 29 (12), 2363–2373.

Klaseboer, E., Chevaillier, J.P., Gourdon, C., Masbernat, O., 2000. Film drainage between colliding drops at constant approach velocity: experiments and modeling. J. Colloid Interface Sci. 229 (1), 274–285.

Ladyzhenskaya, O.A., 1969. The Mathematical Theory of Viscous Incompressible Flow, 76.

Lee, J.C., Hodgson, T.D., 1968. Film flow and coalescence-i basic relations, film shape and criteria for interface mobility. Chem. Eng. Sci. 23 (11), 1375–1397.

Lehr, F., Millies, M., Mewes, D., 2002. Bubblesize distributions and flow fields in bubble columns. AIChE J. 48 (11), 2426–2443.

Liao, Y., Lucas, D., 2010. A literature review on mechanisms and models for the coalescence process of fluid particles. Chem. Eng. Sci. 65 (10), 2851–2864.

Oron, A., Davis, S.H., Bankoff, S.G., 1997. Long-scale evolution of thin liquid films. Rev. Mod. Phys. 69 (3), 931.

Orvalho, S., Ruzicka, M.C., Olivieri, G., Marzocchella, A., 2015. Bubble coalescence: effect of bubble approach velocity and liquid viscosity. Chem. Eng. Sci. 134, 205–216.

Patera, A.T., 1984. A spectral element method for fluid dynamics: laminar flow in a channel expansion. J. Comput. Phys. 54 (3), 468–488.

Saboni, A., Gourdon, C., Chesters, A.K., 1995. Drainage and rupture of partially mobile films during coalescence in liquid-liquid systems under a constant interaction force. J. Colloid Interface Sci. 175 (1), 27–35.

Scott, M.A., Simpson, R.N., Evans, J.A., Lipton, S., Bordas, S.P., Hughes, T.J., Sederberg, T.W., 2013. Isogeometric boundary element analysis using unstructured t-splines. Comput. Methods Appl. Mech.Eng. 254, 197–221.

Shinnar, R., 1961. On the behaviour of liquid dispersions in mixing vessels. J. Fluid Mech. 10 (2), 259–275.

Shinnar, R., Church, J.M., 1960. Statistical theories of turbulence in predicting particle size in agitated dispersions. Ind. Eng. Chem. 52 (3), 253–256.

Yaminsky, V.V., Ohnishi, S., Vogler, E.A., Horn, R.G., 2010. Stability of aqueous films between bubbles. Part 1. The effect of speed on bubble coalescence in purified water and simple electrolyte solutions. Langmuir 26 (11), 8061–8074.

Yiantsios, S.G., Davis, R.H., 1990. On the buoyancy-driven motion of a drop towards a rigid surface or a deformable interface. J. Fluid Mech. 217, 547–573.

Yiantsios, S.G., Davis, R.H., 1991. Close approach and deformation of two viscous drops due to gravity and van der waals forces. J. Colloid Interface Sci. 144 (2), 412–433.